

# Large-Scale Flow Response to Short Gravity Waves Breaking in a Rotating Shear Flow

FRANÇOIS LOTT

*Laboratoire de Météorologie Dynamique du CNRS, Ecole Normale Supérieure, Paris, France*

(Manuscript received 17 January 2002, in final form 22 January 2003)

## ABSTRACT

A two-dimensional rotating anelastic model is used to analyze the large-scale flow (LSF) response to the breaking of gravity waves (GWs) at critical levels. In the response the balanced part is separated from the inertial oscillations (IOs) and the inertia-gravity waves (IGWs). Interest also focuses on the relative importance of the two, when the regime of the critical levels interaction becomes nonlinear.

In the linear periodic case, the balanced response is a mean transverse velocity that equilibrates the wave drag via the Coriolis torque, and the unbalanced one is an IO. Their relative importance is well predicted by a temporal Rossby number associated with the timescale of the GWs forcing onto the mean flow. When the dynamics are nonlinear, the GWs are reflected by the shear layer, affecting the GWs' forcing amplitude. A nonlinear feedback loop also makes the ratio between the IO and the balanced response much larger than in the linear case.

In the nonperiodic case, the balanced motion is a growing baroclinic pattern, which results from steering by the shear of the potential vorticity (PV) dipole generated where the GWs break. The unbalanced response consists of IGWs propagating away from the shear layer. Contrary to the periodic case, the ratio between the two is not much affected by nonlinearities, and stays well predicted by a spatial Rossby number associated with the spatial scale of the GWs forcing on the LSF. When this number is near 1, and the interaction nonlinear, the IGWs outside of the shear layer make a substantial fraction of the total wave signal.

## 1. Introduction

The large-scale flow (LSF) response to the breaking of vertically propagating gravity waves (GWs) with short horizontal wavelength has been the subject of many studies during the last 40 years. They follow the seminal works of Eliassen and Palm (1961) and Bretherton (1969), which have shown that mountain GWs induce a net transfer of momentum from the ground toward the atmosphere. The fact that breaking GWs is important to the general circulation of the atmosphere is now well established (Palmer et al. 1986; Holton 1982).

In mesoscale and synoptic-scale meteorology the momentum deposit by GWs is also an important process. In the 2D context, the breaking of mountain GWs can help the development of downslope windstorms, by producing, below where they break, a resonant cavity for all the disturbances generated by the mountain (Smith 1985). This process becomes very efficient when the mountain GWs break at a critical level, a situation where the flow response is extremely sensitive to the height

of the space between the critical level and the ground [Clark and Peltier (1984); see also Bacmeister and Pierrehumbert (1988) for a comparison between the theories of Smith (1985) and Clark and Peltier (1984)]. The nonlinear dynamics of mountain GWs can also lead to the development of larger-scale disturbances, that spread in time, and build up a blocked flow region upstream of the obstacle (Pierrehumbert and Wyman 1985).

For 3D obstacles, the breaking of GWs induce downstream wakes (Miranda and James 1992; Schär and Durran 1997) that are well described by the potential vorticity (PV) produced by the GWs' momentum deposit.

It is noteworthy that 2D and 3D studies complement one another. On the one hand, the 2D studies emphasize and probably overstate, by construction, that part of the LSF response that cannot be described using PV, and that is made in part of long secondary GWs. These long disturbances make up the flow dynamics near the obstacle. The 3D studies, based on PV diagnostics, eventually illustrate with less ambiguity the nature of the interaction between the primary GWs and the large-scale flow. The PV produced by breaking GWs can influence the flow dynamics far downstream from the obstacle.

Compared to studies about the impact of GWs on the zonal mean flow (Palmer et al. 1986), it is noteworthy

---

*Corresponding author address:* Dr. François Lott, Laboratoire de Météorologie Dynamique du CNRS, Ecole Normale Supérieure, 24, Rue Lhomond, Paris Cedex 05 F75231, France.  
E-mail: Llott@lmd.ussieu.fr

that most studies about the impact of GWs breaking on the regional circulation often neglect the Coriolis force. This is not justified in many circumstances, and again, the example of mountain waves is instructive. Indeed, the ageostrophic forcing they induce on the LSF is well known through records of the surface pressure drag. As noticed by Scavuzzo et al. (1998), the drag measured along a  $L = 150$ -km-long transect across the Pyrénées (Bessemoulin et al. 1993) presents narrow peaks of less than  $T = 1$  day. At these space scales and timescales, the temporal and spatial Rossby numbers

$$\epsilon_r = \frac{1}{fT} \quad \text{and} \quad \epsilon_L = \frac{U_0}{fL}, \quad (1)$$

are near 1, indicating that the LSF response to the GWs' drag is influenced by the Coriolis torque. In Eq. (1),  $f$  is the Coriolis parameter and  $U_0$  is a characteristic wind speed. In the rest of the paper  $L$  and  $T$  will indicate the characteristic space scales and timescales at which the GWs affect the LSF.

A convenient framework to address the LSF response at these temporal and spatial scales is that of the geostrophic adjustment theory. It shows that an initial distribution of mass and momentum evolves by radiating inertia-gravity waves (IGWs) toward a balanced state fully described by the initial PV distribution (Rossby 1937; Blumen 1972; Fritts and Luo 1992). The nonlinear mechanisms that produce the imbalance can be strong during the life cycle of barotropic and baroclinic instabilities (Ford 1994; O'Sullivan and Dunkerton 1995), as well as during fast frontogenesis (Reeder and Griffiths 1996). With the Rossby numbers evaluated with the Pyrénées Experiment (PYREX) data being near 1 (Scavuzzo et al. 1998), it is evident that GWs breaking is another major source of imbalance. In response, the large-scale flow adjusts, as witnessed by the presence of large IGWs near the Pyrénées during events where the pressure drag evolves on a timescale that compares with  $1/f$  (Scavuzzo et al. 1998).

Momentum deposition due to short GWs as a potential source of secondary IGWs has been investigated by Vadas and Fritts (2001). These authors considered the linear response to a prescribed momentum deposition that acts at all spatial and temporal scales. With a comparable linear approach, Buhler et al. (1999) noticed that the initial imbalance that induces IGWs can be due to the mixing associated with Kelvin-Helmholtz instabilities. Nevertheless, there are few nonlinear studies in the rotating case that describe the GWs breaking together with its LSF response.

In the present paper we describe the LSF response to GWs breaking in the fully nonlinear rotating case, and with particular attention given to (a) the partition between the balanced response and the IGWs/internal oscillations (IOs) in the LSF response, and to (b) the possible nonlinear feedbacks between the LSF response and the GW forcing. Because this problem embraces a very

large range of scales, from the very small scales of turbulence to the few hundred kilometers characterizing the Rossby radius of deformation, and this is true as well for the temporal scales, the computational overhead makes it untreatable at reasonable cost. To circumvent this difficulty we formulate the problem by making a series of simplifications.

First, we assume that the dynamics stays two-dimensional (2D) all of the time, which we know is not valid when GWs break (Fritts et al. 1996; Afanasyev and Peltier 2001). We circumvent that difficulty by imposing that the GWs break at well-identified critical levels where the dynamics are controlled by artificially high viscosity (see appendixes A and B). During GWs breaking, it dissipates the Kelvin-Helmholtz instabilities before they lead to 3D convective overturning. To impose the presence of critical levels, we consider near-steady gravity waves and specify a background flow

$$U(z) = U_0 \tanh[(z_c - z/D)],$$

$$N^2(z) = \frac{g}{\theta_0} \frac{d\theta_0}{dz} = N_0^2 = \text{const}, \quad (2)$$

whose velocity reverses sign at a given altitude  $z_c$ . In Eq. (2),  $U(z)$  is the plane-parallel background velocity,  $D$  is the shear layer depth,  $N$  is the Brunt-Väisälä frequency,  $\theta_0(z)$  is a background potential temperature profile, and  $g$  is the gravitational acceleration. Note as well that the thermal wind balance imposes the presence of a second background potential temperature

$$\Theta(y, z) = -\frac{f\theta_0(z)}{g} \frac{dU}{dz} y, \quad (3)$$

where  $y$  is the direction perpendicular to the 2D plane of interest here.

Another difficulty is that no disturbance can stay 2D when the background wind shear varies with altitude. Nevertheless, they can be forced to stay 2D by neglecting  $\Theta_z w$  in front of  $\theta_{0z} w$  in the thermodynamic equation, where  $w$  is the vertical velocity. This approximation is only valid when the background Richardson number is large everywhere (see appendix A). Note also that this approximation does not preclude the derivation of consistent GW-LSF interaction diagnostics, such as (a) Eliassen-Palm flux transformed Eulerian mean flow budgets (Andrews and McIntyre 1976), (b) PV budgets (Haynes and McIntyre 1987), and (c) disturbance energy budgets.

Another difficulty is that the background flow (2) supports baroclinic instabilities. To limit their importance in the LSF evolution, we impose that the background minimum Richardson number  $\text{Ri}_m = N_0^2 D^2 / U_0^2 \gg 1$ , so only long baroclinic instabilities can develop; none of the imposed GWs correspond to unstable modes. For the LSF, the onset of baroclinic instabilities is also limited by (a) the rather small size of the domain and (b) the presence of lateral sponge layers where linear

damping coefficients far exceed the characteristic baroclinic instability growth rate.

Section 2 presents the interaction between a monochromatic GW and a shear layer in the periodic case. The domain length equals the GW horizontal wavelength. The LSF is the horizontally averaged flow. In the response we distinguish between a balanced flow that equilibrates the GW drag via the Coriolis force and inertial oscillations. Section 3 presents the interaction between a narrowband (in the parallel  $x$  direction) packet of GWs and the LSF. In this case the large-scale flow is defined via a low-pass filter that excludes all the GWs. In the LSF the balanced part is deduced from the PV field, and the IGWs are identified in the far field. Section 4 presents some conclusions.

## 2. Periodic cases

### a. Heuristic solution

In a periodic domain, and assuming that a GW deposits momentum in a zone of limited vertical extent, the mean flow response is driven by the forced inertial oscillator equations:

$$\begin{aligned} \frac{\partial \langle \rho_0 \bar{u} \rangle}{\partial t} - f \langle \rho_0 \bar{v}^* \rangle &= \langle \bar{F}_x \rangle, \\ \frac{\partial \langle \rho_0 \bar{v}^* \rangle}{\partial t} + f \langle \rho_0 \bar{u} \rangle &= 0. \end{aligned} \quad (4)$$

In Eq. (4), the overbar corresponds to the usual along- $x$  mean, the star corresponds to the transformed Eulerian mean formalism (Andrews and McIntyre 1976), and the  $\langle \rangle$  correspond to a vertical averaging, which are upper and lower limits, dubbed, at least, the region where the GW breaks. When the momentum deposit  $\langle \bar{F}_x \rangle$  varies in time with a timescale  $T$  that is slow compared to  $1/f$ , the response in Eq. (4) is near

$$\langle \rho_0 \bar{v}_b \rangle = -\langle \bar{F}_x \rangle / f. \quad (5)$$

In Eq. (5), the subscript  $b$  denotes “balanced” in the sense that  $\langle \rho_0 \bar{v}_b \rangle$  is given by a diagnostic equation. In this balanced response a wave-induced deceleration is equilibrated by a positive transverse motion. When  $\epsilon_T \approx 1$ , the solution to Eqs. (4) differs significantly from  $\langle \rho_0 \bar{v}_b \rangle$ . As an example, if a forcing  $\langle \bar{F}_x \rangle$  starts at  $t = 0$  varies like

$$\begin{aligned} -\frac{F_0}{2} [1 - \cos(t/T)] &\quad \text{for } 0 < t < \pi T, \quad \text{and} \\ -F_0 &\quad \text{for } t > \pi T, \end{aligned} \quad (6)$$

and alters a flow that is initially at rest, the solution for  $t > \pi T$  is

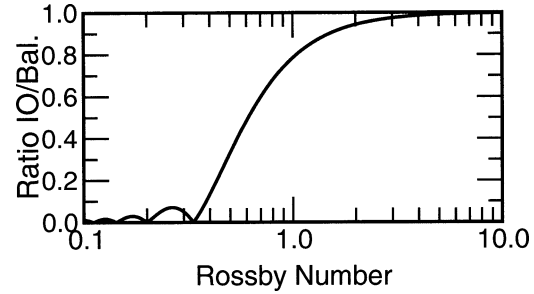


FIG. 1. Simple example of the adjustment to a specified momentum deposit. Ratio between the IO amplitude and the balanced solution for  $t > \pi T$  and as a function of the Rossby number.

$$\begin{aligned} \langle \rho_0 \bar{v}^* \rangle = \frac{F_0}{f} - \frac{F_0}{2f} \frac{\epsilon_T^2}{\epsilon_T^2 - 1} \left[ \left( 1 + \frac{\cos \pi}{\epsilon_T} \right) \cos ft \right. \\ \left. + \frac{\sin \pi}{\epsilon_T} \sin ft \right]. \end{aligned} \quad (7)$$

The first terms on the right-hand side of Eq. (7) is the balanced solution [Eq. (5)], and the second is an IO.

The ratio between the IO and the balanced response in Eq. (7) is plotted for different values of the parameter  $\epsilon_T$  in Fig. 1. When the Rossby number  $\epsilon_T > 1$ , the balanced solution is a poor approximation of the complete solution, and the amplitude of the inertial oscillation is comparable to that of the balanced mean transverse velocity. When  $\epsilon_T \ll 1$  the balanced solution approximates very well the solution.

### b. Numerical experiment setup

To treat the periodic case with more details, we use the 2D anelastic model described in appendix A. The background flow (2) parameters are  $U_0 = 10 \text{ m s}^{-1}$ ,  $D = 2500 \text{ m}$ ,  $N_0^2 = 1.10^{-4} \text{ s}^{-2}$ ,  $f = 1.09 \cdot 10^{-4} \text{ s}^{-1}$ , and  $z_c = 10 \text{ km}$ . For this flow, the minimum background Richardson number  $\text{Ri}_m = (N^2/U_z^2)(z_c) = 6.25$ , and the inertial period,  $2\pi/f = 16 \text{ h}$ . In all the simulations the domain total height is 25 km and a damping layer lies above  $z_T = 20 \text{ km}$  (Fig. 2). The model grid has  $N = 306$  points in the vertical direction, and the vertical grid spacing varies with altitude to ensure good resolution at the critical levels (see appendix B for a comparison between  $dz$  and the length scales of the GW–critical level interaction). Accordingly, the grid spacing is constant and equals  $dz_{\min} = 30 \text{ m}$  when  $z_c - D < z < z_c + D$ . It equals  $dz_{\max} = 250 \text{ m}$  when  $0 \text{ km} < z < z_c - 2D$  and when  $z = z_c + 2D < z < 25 \text{ km}$ . Here  $dz$  varies as a cosine function of altitude in the intervals  $z_c - 2D < z < z_c - D$  and  $z_c + D < z < z_c + 2D$ , in order to ensure smooth transitions between  $dz_{\max}$  and  $dz_{\min}$ .

We consider a domain of length  $L_D = 30 \text{ km}$  and the truncation in the horizontal direction is  $M = 64$ , a value for which model convergence was verified. To impose

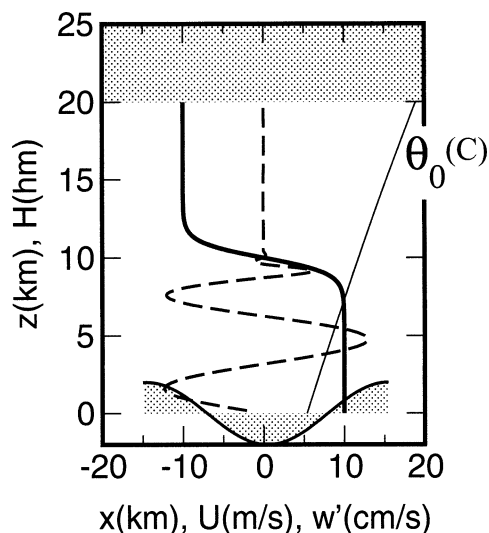


FIG. 2. Typical model configuration in the periodic case. Corrugated bottom  $H(x)$  (thick solid line and filled area); background parallel velocity  $U(z)$  (thick solid line); potential temperature profile of the fluid at rest  $\theta_0(z)$  (thin solid line); wave vertical velocity  $w'(0, z)$  (thick dashed line). The gray zone above  $z = 20$  km indicates the sponge layer.

a periodic wave, the corrugated bottom  $H(x)$  [Eq. (A7) in appendix A] is

$$H(x) = H_0 \cos(2\pi x/L_D), \quad (8)$$

where  $H_0$  controls the GW amplitude. All the simulations presented last 96 h.

### c. Near-linear regime, $H_0 = 1$ m

To analyze the wave–mean flow interaction we form the transformed Eulerian mean of the 2D anelastic Eqs. (A3)–(A4) in appendix A (Andrews and McIntyre 1976):

$$\rho_0 \bar{u}_t - \rho_0 f \bar{v}^* = -\partial_z(\rho_0 \bar{u}' w') - \rho_0 f \bar{\theta}' v' / \theta_{0z} + \partial_z \mu \partial_z \bar{u} = \bar{F}_x, \quad (9)$$

$$\rho_0 \bar{v}^*_t + \rho_0 f \bar{u} = -\partial_z[\rho_0 \bar{v}' w' + \partial_t(\rho_0 \bar{\theta}' v' / \theta_{0z})] + \partial_z \mu \partial_z \bar{v} = \bar{F}_y, \quad (10)$$

$$\rho_0 \bar{\theta}_t + \rho_0 \bar{v}^* \bar{\Theta}_y = -\partial_z(\rho_0 \bar{\theta}' w') - \Theta_y \rho_0 \bar{\theta}' v' / \theta_{0z} + \partial_z \kappa \partial_z \bar{\theta} = \bar{H}. \quad (11)$$

In Eqs. (9)–(11), the prime denotes the departure from the mean flow, and the residual mean transverse velocity  $\bar{v}^* = \bar{v} - (1/\rho_0)(\rho_0 \bar{\theta}' v' / \theta_{0z})_z$ . Figure 3a shows the vertical profiles of the GW forcings  $\bar{F}_x$ ,  $\bar{F}_y$  and  $\bar{H}$  in Eqs. (9)–(11) at  $t = 40$  h and when  $H_0 = 1$  m. In this case, the critical-level regime is near linear (see appendix B), so the GW fields become steady after 24 h of integration and stay unchanged at least until  $t = 96$  h. Figure 3a shows that the dominant effect of the wave is to de-

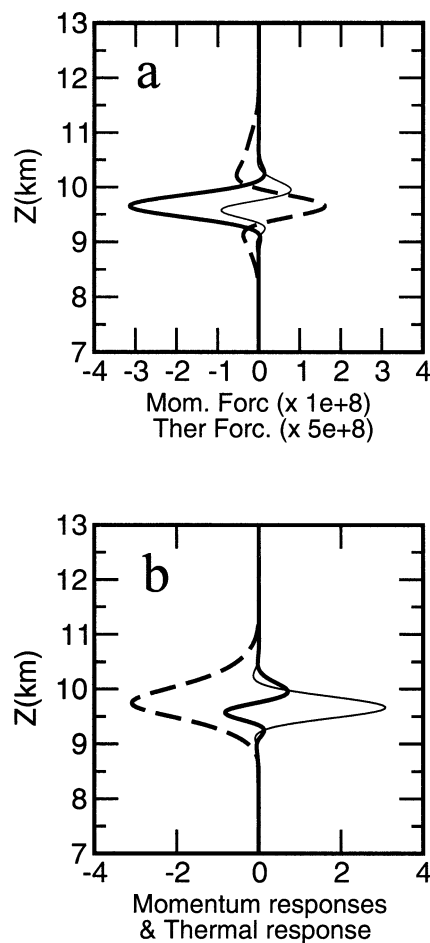


FIG. 3. Periodic “linear” case:  $H_0 = 1$  m. (a) Vertical profiles of the mean flow forcings at  $t = 40$  h: parallel momentum forcing  $\bar{F}_x$  (thick solid line), transverse momentum forcing  $\bar{F}_y$  (thin solid line), and thermal forcing  $\bar{H}$  (thick dashed line);  $\bar{F}_x$  and  $\bar{F}_y$  are multiplied by  $10^8$ ,  $\bar{H}$  is multiplied by  $5 \cdot 10^8$ . (b) Vertical profiles of the mean flow responses averaged in time between  $t = 32$  h and  $t = 48$  h: parallel wind  $\bar{u}(z)$  (thick solid line), transverse wind  $\bar{v}^*(z)$  (thin solid line), and potential temperature  $\bar{\theta}(z)$  (thick dashed line); all values are multiplied by  $10^4$ .

celerate the mean flow in the  $x$  direction:  $\bar{F}_x$  (thick solid in Fig. 3a) is negative over a 1-km-deep layer located below  $z_c = 10$  km, and is very small elsewhere. The transverse forcing  $\bar{F}_y$  (thin solid in Fig. 3a) is positive around and just below 10 km and becomes negative below 9.75 km. Integrated vertically and over the shear layer it is null, which naturally follows that the wave drag is oriented in the  $x$  direction. As  $\bar{F}_y$ , the thermal forcing  $\bar{H}$  makes no net contribution (thick dashed in Fig. 3a), it presents a maxima near 9.75 km surrounded by two minima at  $z = 9$  km and  $z = 10$  km, respectively.

The mean flow responses to these forcings that do not contain IOs are shown in Fig. 3b at  $t = 43$  h. In this figure, the IOs are filtered out by averaging in time and over one inertial period the instantaneous mean flow profiles  $\bar{u}(z)$ ,  $\bar{v}^*(z)$ , and  $\bar{\theta}(z)$ . Figure 3b shows that the transverse flow response  $\bar{v}^*(z)$  has increased nearly ev-

erywhere in the lower part of the shear layer (i.e., between  $z = 9$  km and  $z = 10$  km; thin solid in Fig. 3b) to equilibrate  $\overline{F_x}(z)$  via the Coriolis torque. In the same space, the potential temperature has decreased everywhere (thick dashed line in Fig. 3b). Since this net and negative potential temperature pattern cannot result from a direct thermal forcing (thick dashed line in Fig. 3a), it can only be induced by the transverse flow, and through the transverse advection term  $\rho_0 \overline{v^* \Theta_y}$  [Eq. (11)].

Note also that in the long term, the mean flow profile  $\overline{\theta}(z)$  in Fig. 3b never reaches a limit profile (not shown):  $\overline{\theta}$  continuously decreases in response to  $\rho_0 \overline{v_b \Theta_y}$ . In the long term, this causes the shear layer to become convectively unstable everywhere,  $\theta_{0z} + \overline{\Theta}_z < 0$ , a situation we do not discuss in this paper. By contrast with the other two mean flow profiles, the parallel mean velocity  $\overline{u}(z)$  presents no net modification (solid line in Fig. 3b): it is positive around  $z = 10$  km but negative around  $z = 9.5$  km.

A concise way to address the net effect of the wave on the mean flow is to form an absolute angular momentum budget by integrating vertically the Eqs. (9)–(10) over the shear layer depth (i.e., from  $z_c - D$  up to  $z_c + D$ ). It results exactly in the heuristic model Eqs. (4) with

$$\langle \overline{F_x} \rangle = - \left[ \rho_0 \overline{u' w'} - \rho_0 f \frac{\overline{\theta' v'}}{\theta_{0z}} \right]_{z_c - D}^{z_c + D}, \quad (12)$$

and after verification, the diffusive fluxes of momentum through  $z = z_c - D$  and  $z = z_c + D$  are very small.

Figure 4a shows the temporal evolution of the waveforcing  $\langle \overline{F_x} \rangle$  for different values of  $H_0$ . In the linear case (thin solid line in Fig. 4a)  $\langle \overline{F_x} \rangle$  becomes constant after  $t = 4$ –5 h and near equal and oppositely signed to the hydrostatic-Boussinesq linear nonrotating mountain GW drag  $D_r = \rho_0(1)(\pi/L_D)NU_0H_0^2$ . From this temporal evolution we can deduce the forcing timescale  $T$  that best fits the timescale in the heuristic model forcing [Eq. (6)]:  $\pi T = 4$ –5 h. In this case, the Rossby number  $\epsilon_r \approx 2$ , and we can expect that the inertial oscillation amplitude compares to that of the balanced motion [Fig. 1 and Eq. (5)].

This is verified in Fig. 4b in which the left curve shows the hodograph of the mean momentum vector

$$\langle \langle \rho_0 \overline{u} \rangle; \langle \rho_0 \overline{v^*} \rangle \rangle \quad (13)$$

and the entire duration of the model integration. The hodograph is a circle in which the ray approximately equals the balanced solution amplitude (the linear balanced solution is indicated by the cross in Fig. 4b); each circumvolution around this circle is made within a period nearly equal to the inertial period.

#### d. Nonlinear regime: $H_0 = 80$ m

When  $H_0$  increases, the GW dynamics becomes nonlinear and the GW becomes sensitive to the mean flow

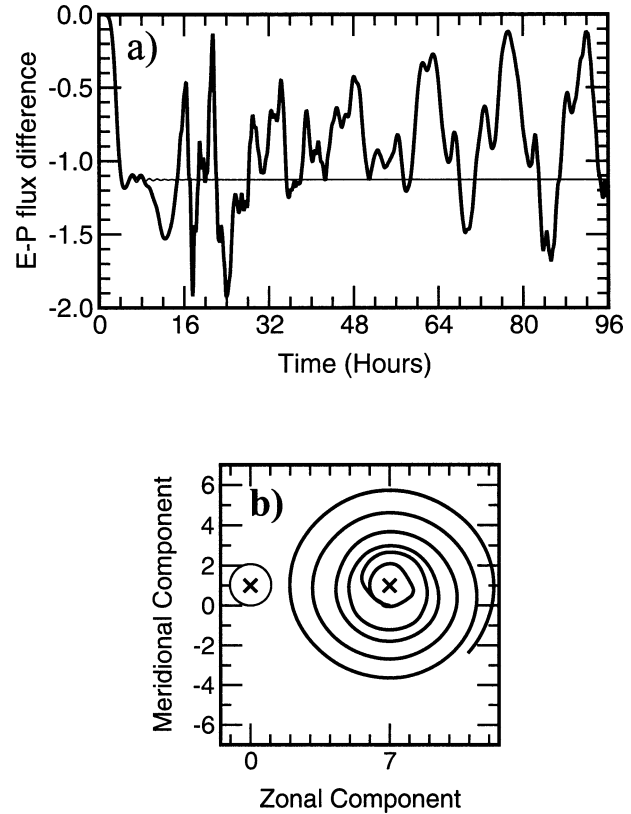


FIG. 4. (a) Eliassen–Palm flux difference between both sides of the shear layer. All values are divided by  $D_r = \rho_r(\pi/L_D)NU_0H_0^2$ . (b) Hodograph of the mean momentum vector averaged over the shear layer depth. All values are divided by  $D_r/f = \rho_r(\pi/fL_D)NU_0H_0^2$ . The right hodograph in (b) is translated horizontally for clarity and the crossed symbols indicate the location of the linear steady response to a constant forcing of value  $D_r$ . Here,  $H_0 = 1$  m (thin solid line) and  $H_0 = 80$  m (thick solid line) in both (a) and (b).

changes it induces. To numerically address this transition we perform successive experiments, increasing  $H_0$ , and present the case where  $H_0 = 80$  m. The thick solid line in Fig. 4a shows that the waveforcing  $\langle \overline{F_x} \rangle$  decreases within 5–6 h down to near minus the linear GW drag, and then starts to vary around that linear value. In the long term, its variations get locked with the inertial oscillation: the time lag between two maxima (or two minima) in  $\langle \overline{F_x} \rangle$  after  $t = 50$  h, being near 16 h. As a consequence, the amplitude of the IO (thick solid line in the right of Fig. 4b) becomes very large, compared to the linear balanced response (again, indicated by a “+”) and to the inertial oscillation in the linear case: the inertial oscillator [Eq. (4)] is excited by a forcing  $\langle \overline{F_x} \rangle$  that has significant power near  $f$ .

In the establishment of this resonant feedback, the nonlinear reflections of the incident GW play a central role. In the nonrotating case, it is well established that they essentially result from the changes in the wind shear intensity just below the critical levels. In this case,  $\overline{F_x}$  modifies the parallel velocity  $\overline{u}(z)$ , induces a regular descent of the critical level, and produces sharp wind

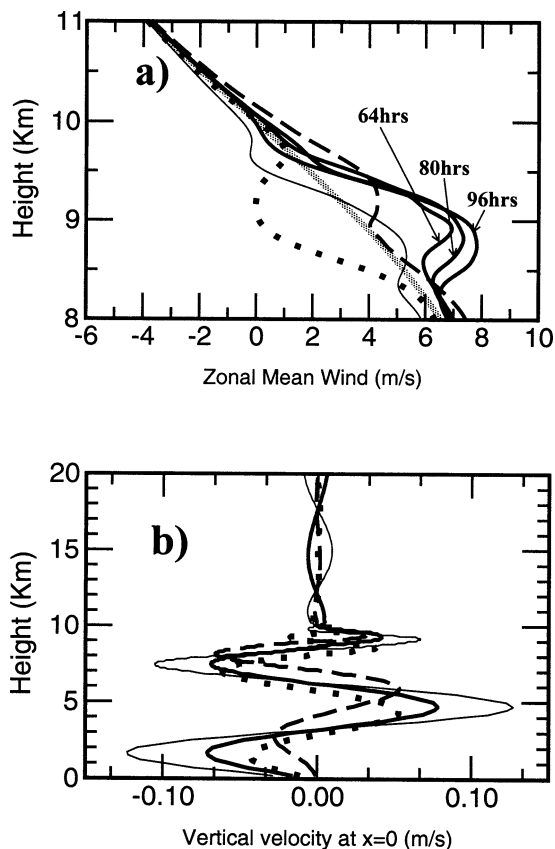


FIG. 5. Temporal evolution of the mean flow and of the wave field in the periodic case, and for  $H_0 = 80$  m. (a) Background flow  $U(z)$  (thick gray line) and total parallel mean flow  $U(z) + \bar{u}(z)$ : thick solid line is  $t = 64, 80$  and  $96$  h; thin solid line is  $t = 84$  h; thick dotted line is  $t = 88$  h; thick dashed line is  $t = 92$  h. (b) Wave vertical velocity: thick solid line is  $t = 80$  h; thin solid line is  $t = 84$  h; thick dotted line is  $t = 88$  h; thick dashed line is  $t = 92$  h.

shears below this level (Fritts 1978; Lott and Teitelbaum 1992). As shown before, with rotation,  $\overline{F}_x$  induces a transverse velocity, so the net effect on the horizontal velocity is perpendicular to that expected in the non-rotating case. An eventually more spectacular difference is that with Coriolis force, the mean flow response experiences inertial oscillations that modulate the mean flow profiles.

As an illustration of this, Fig. 5a presents the profiles of the mean parallel flow  $U(z) + \bar{u}(z)$  at three successive times, each separated by 16 h (thick solid lines in Fig. 5a) and at three successive times each separated by 4 h (thin–thick dashed, and thick long-dashed lines in Fig. 5a). These curves show that the mean flow varies more within one inertial oscillation period than from one period to the next. For instance, at  $t = 80$  h, the phase of the inertial oscillation is such that the mean flow  $U(z) + \bar{u}(z)$  is larger everywhere than the initial background flow  $U(z)$ . If we assume that the altitude  $z_b$ , where  $U(z_b) + \bar{u}(z_b) = 0$ , indicates the upper bound of the area where the GW is absorbed and/or reflected, it is near  $z_b = 10$

km at  $t = 80$  h. Four hours later ( $t = 84$  h; thin solid line in Fig. 5a), the mean parallel flow has decreased everywhere, and  $z_b \approx 9.5$  km. Another 4 h later ( $t = 88$  h; thick dotted line in Fig. 5a),  $U(z) + \bar{u}(z)$  is smaller than the background flow and  $z_b \approx 9$  km everywhere. Thereafter, the flow increases and  $z_b$  returns above  $z = 10$  km ( $t = 92$  h; thick long dashed in Fig. 5a). As a result of these inertial oscillations in the altitude where the GW interact with the critical level, it is likely that the phase of the reflected GW will vary at that periodicity. Furthermore, as these oscillations are related to important wind shear variations, we can expect that the amplitude of the reflected GW will also vary.

This point has been verified by looking at the amplitude and the phase of the reflected GW, below the shear layer (Fig. 5b). For this diagnostic, we write the GW vertical velocity below the shear layer as

$$\begin{aligned} \sqrt{\rho_0(z)}w' \\ \approx \frac{W_0}{\sqrt{\rho_0(z)}} \exp(ikx)[\exp(+imz) + R \exp(-imz) \\ - R \exp(+imz)], \end{aligned} \quad (14)$$

where  $R$  is a complex reflection coefficient. The evaluation of  $R$  from the model outputs gives, for its real part,  $R_r \approx 0, -0.25, 0.23,$  and  $0.5$  at  $t = 80, 84, 88,$  and  $92$  h, respectively. From Eq. (14), these values can be related to  $\langle \overline{F}_x \rangle$  by the approximate relationship

$$\langle \overline{F}_x \rangle \approx -\rho_r N \pi L_D U_0 H_0^2 (1 - 2R_r). \quad (15)$$

Equation (15) with the values of  $R_r$  given above is entirely consistent with  $\langle \overline{F}_x \rangle$ , which is near its negative linear value at  $t = 80$  h (thick solid line in Fig. 4a); has a pronounced negative minimum at  $t = 84$  h; and is near zero at  $t = 92$  h.

### 3. Nonperiodic case

In the nonperiodic case, the large-scale forcing has finite horizontal scale and can induce IGWs propagating away from the area where the GWs critical level interaction occurs. In this case, the degree of imbalance is not only given by  $\epsilon_r$  but also by  $\epsilon_L$  [Eq. (1)].

#### a. Experiments setup

In all the simulations presented next, the domain extends between  $x = 300$  km and  $x = 600$  km, and the layer between  $x = 300$  km and  $x = 600$  km is occupied by a sponge layer to damp all disturbances that pass through the lateral boundaries. In most cases, the model truncation in the horizontal direction is  $M = 768$ , a value for which model convergence was verified by making sensitivity tests varying the horizontal resolution. The vertical structure is as in section 2, and the simulations last 30 h.

To set up a framework that allows us to distinguish

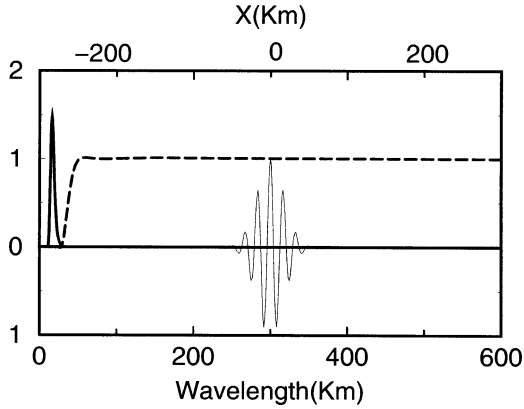


FIG. 6. Horizontal domain and GW forcing characteristics in the non periodic case. Corrugated bottom  $H(x)$  (light solid line); power spectrum of  $H(x)$ ,  $\hat{H}\hat{H}^*(k)$  (thick solid line); transfer function of the low-pass filter  $\hat{K}\hat{K}^*(k)$  (thick dashed line).

the LSF from the GWs, we specify a corrugated bottom with a well-defined spectral low-frequency cutoff:

$$H(x) = H_0 \exp\left(-\frac{x^2}{L_H^2}\right) \cos\left(\frac{3\pi x}{L_H}\right), \quad (16)$$

where  $L_H = 25$  km. Figure 6 shows that the profile (16) mimics a massive mountain of approximate length  $L = 100$  km made of five successive ridges separated by nearly 16.7 km. Its power spectrum  $\hat{H}\hat{H}^*(k)$ , where the hats indicate Fourier coefficients, is narrowband, centered around the horizontal wavelength  $\lambda_x \approx 16.7$  km, and has no power above  $\lambda_x \approx 50$  km (thick solid line in Fig. 6). Accordingly, disturbances with horizontal scales above 50 km will be due only to nonlinear interactions. At these wavelengths, the GWs are near hydrostatics and weakly influenced by rotation, so they experience little horizontal dispersion as they propagate toward the shear layer. Accordingly, we can also use  $L = 100$  km as the horizontal scale to evaluate the spatial Rossby number  $\epsilon_L = U_0/fL = 1$ .

To extract the LSF we apply to the total disturbance fields a nonrecursive low-pass filter  $K(x)$  in the horizontal direction. The filter uses a Kayser window (Hamming 1983, chapters 7 and 9) and is adjusted to minimize Gibbs effects and to have a neat cutoff around  $\lambda_c = 50$  km. Its transfer function  $\hat{K}\hat{K}^*$  is near 1 for all wave-

lengths above  $\lambda_x = 75$  km and near 0 for all wavelengths below  $\lambda_x = 50$  km (thick dashed line in Fig. 6).

To derive diagnostics for the LSF we apply the low-pass filter  $K$  to the anelastic Eqs. (A3)–(A4) in appendix A and write the long disturbance fields evolution:

$$[\partial_t + (U + u_l)\partial_x + w_l\partial_z]\mathbf{u}_l + w_l U_z \mathbf{x} + f\mathbf{z} \wedge \mathbf{u}_l + \nabla\phi_l - g\frac{\theta_l}{\theta_0}\mathbf{z} = \mathbf{F}_l(x, z, t), \quad (17)$$

$$[\partial_t + (U + u_l)\partial_x + w_l\partial_z]\theta_l + \Theta_y v_l + \theta_{0z} w_l = H_l(x, z, t). \quad (18)$$

In Eqs. (17)–(18), the index  $l$  indicates the long disturbance field, so  $\mathbf{F}_l$  and  $H_l$  include, by construction, the diffusion of LSF disturbance fields and the nonlinear interaction between short gravity waves.

### b. Near-linear regime, $H_0 = 15$ m

In the experiment presented in this section, the maximum mountain height is  $H_0 = 15$  m, so the regime of the interaction between the GWs and the shear layer is linear viscous. Accordingly, after a spinup period that lasts less than 6 h, the GWs fields stay near constant throughout the 30-h simulation. At this time the GWs pattern consist of a system of vertically propagating mountain waves that are absorbed within the shear layer (Fig. 7a). The absorption of the GWs below  $z_c$  results a momentum deposit, which gives an LSF forcing in the parallel direction  $F_{xl}$  that is essentially negative within the shear layer (Fig. 7b).

The large-scale flow response to the critical level absorption of the GWs is shown in Fig. 8. Apparent on nearly all fields in Figs. 8a–c, the LSF response at  $t = 6$  h is large inside the shear layer (between  $z = 8$  km and  $z = 12$  km) but also presents a wavelike pattern below  $z = 8$  km. This wave pattern can essentially be seen on  $u_l$  and  $\theta_l$  (Figs. 8a,b), while the transverse velocity field  $v_l$  is dominated by a disturbance confined inside the shear layer (Fig. 8c). The fact that the disturbance field below the shear layer is inclined in the direction of the flow indicates that it is made of IGWs propagating downward.

The structure of the long disturbance fields at  $t = 30$  h is shown in Figs. 8d–f. Below the shear layer, it con-

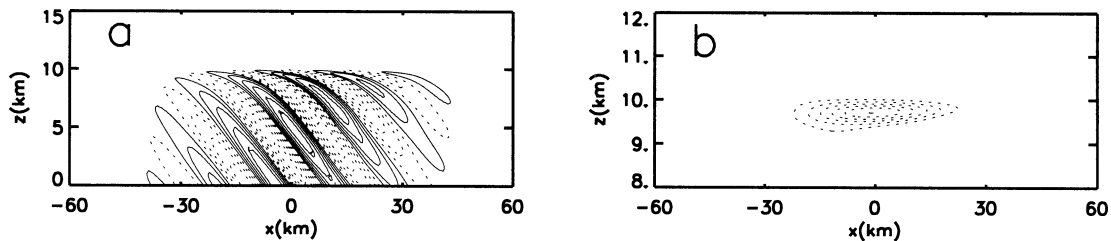


FIG. 7. Nonperiodic simulation with  $H_0 = 15$  m and at  $t = 30$  h. (a) Vertical velocity (contour interval  $0.01$  m s<sup>-1</sup>). (b) Large-scale momentum forcing  $F_{xl}$  (contour interval  $2 \cdot 10^{-6}$  m s<sup>-2</sup>). Negative values are dashed.

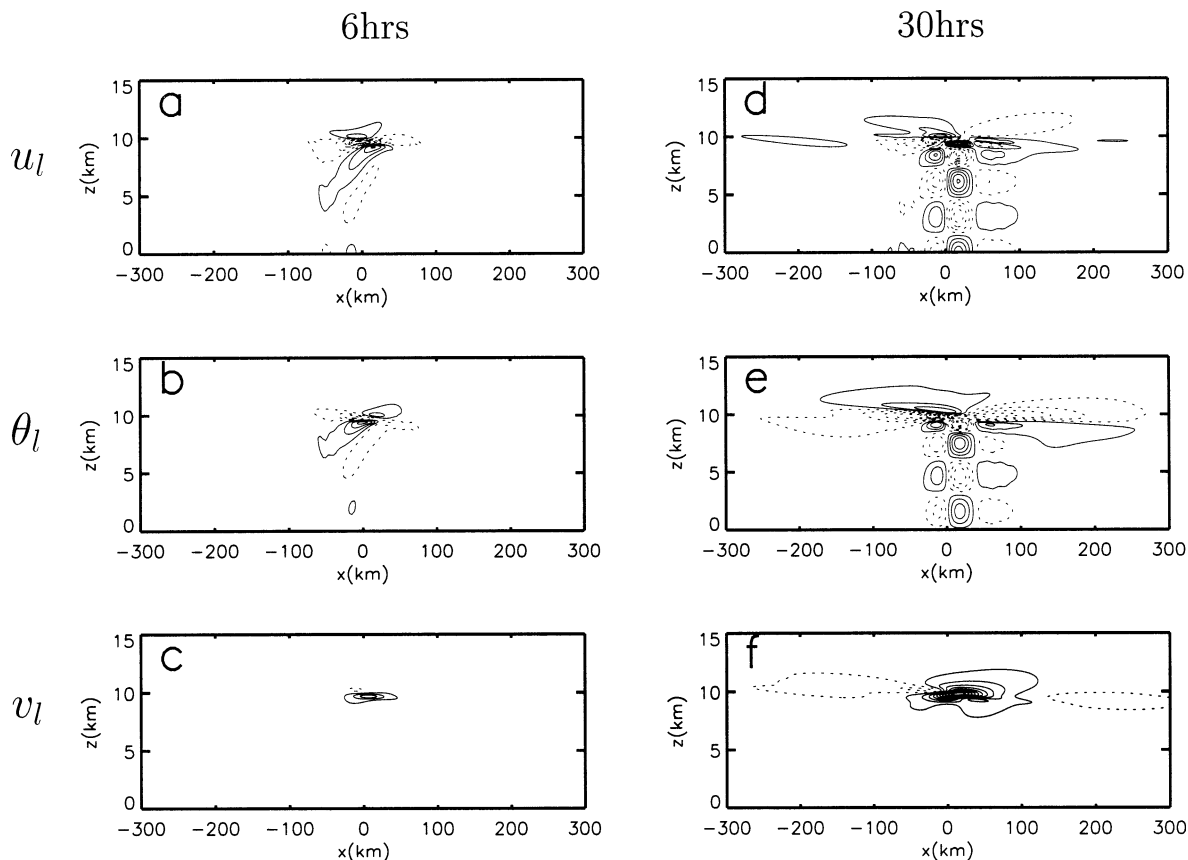


FIG. 8. Nonperiodic case with  $H_0 = 15$  m. LSF disturbance fields at (a)–(c)  $t = 6$  h and (d)–(f)  $t = 30$  h. (a), (d) Parallel wind  $u_l$ ; contour interval is  $5 \times 10^{-3} \text{ m s}^{-1}$ ; (b), (e) Potential temperature  $\theta_l$ ; contour interval is  $2 \times 10^{-3} \text{ K}$ ; (c), (f) transverse wind  $v_l$ ; contour interval is  $10^{-2} \text{ m s}^{-1}$ . Negative values are dashed.

sists of a large-scale standing wave, which results from the superposition of downward IGWs and upward-propagating IGWs of same amplitude (Figs. 8d,e). The downward IGWs are generated in the shear layer, while the upward IGWs result from the total reflection of the downward IGWs at the ground. This standing pattern below  $z = 8$  km becomes steady after  $t = 18$  h, because the reflected upward IGWs are entirely absorbed within the shear layer.

At that time, the LSF transverse velocity presents a large positive pattern (Fig. 8f) centered near  $(x, z) = (0, z_c)$ , and that is confined within the shear layer. The LSF potential temperature also presents, within the shear layer, a pattern that is clearly distinct from the IGWs present below the shear layer (Fig. 8e). Although more complex in structure than the  $v_l$  pattern in Fig. 8f, it is predominantly negative over a long horizontal strip near  $z_c$ . If one follows their evolution in time, the  $v_l$  and the  $\theta_l$  patterns within the shear layer grow steadily.

The balanced part of the flow fields in Fig. 8 is displayed in Fig. 9; they are estimated after inversion of the PV field  $Q_b$  in Figs. 9a,c (see appendix C for the inversion procedure). The balance transverse velocity  $v_b$  (not shown) is very near the long disturbance field

$v_l(x, z)$  displayed at  $t = 6$  h and  $t = 30$  h in Figs. 8c and 8f, respectively. For the potential temperature field, the balanced part is displayed at  $t = 6$  h and  $t = 30$  h in Figs. 9b and 9d, respectively. Comparison between these fields and the large-scale flow fields in Figs. 8b and 8e clearly shows an excellent agreement within the shear layer.

The fact that the balanced response stays confined within the shear layer follows that the disturbance potential vorticity stays confined there as well. For instance, the potential vorticity field at  $t = 6$  h (Fig. 9a) is a dipole pattern with a positive lobe standing above a negative one. This near-exact balance between the negative lobe and the positive one follows that the breaking GWs induce a nonadvective potential vorticity flux,  $\mathbf{J}_N \approx -F_{lx} \Theta_y \mathbf{e}_z$  (see appendix C), oriented upward, because  $F_{lx}$  is negative and  $\Theta_y$  is positive inside the shear layer. As time increases (Fig. 9c), this PV-dipole is steered by the background shear, with the negative PV lobe advected downstream, and the positive one advected upstream.

A more quantitative way to evaluate the partition between balanced flow and IGWs in the response is to evaluate the total disturbance energy:

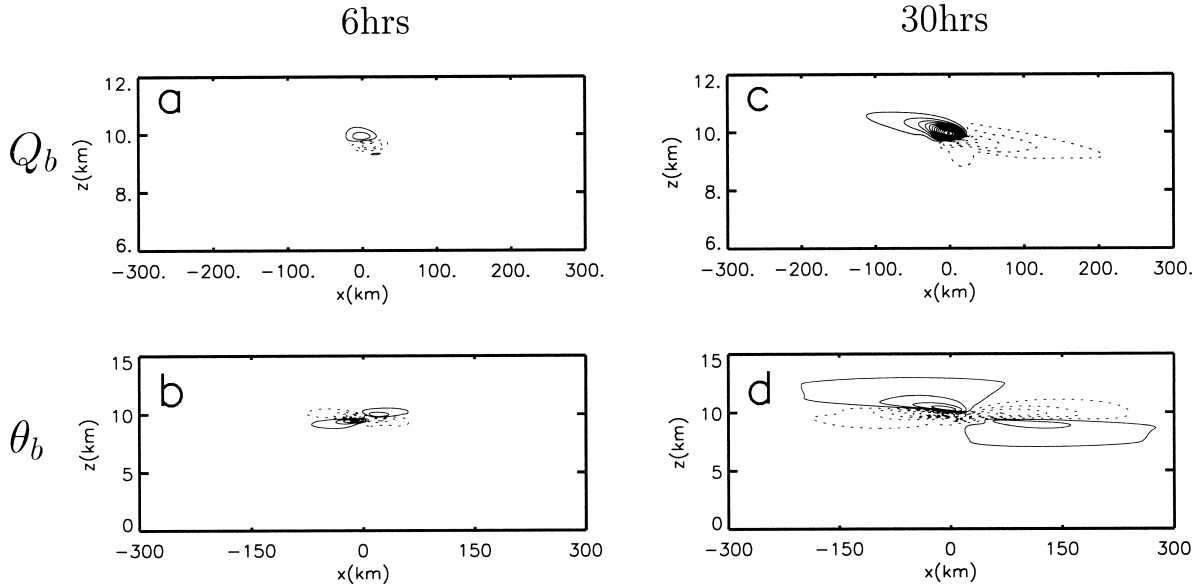


FIG. 9. Same as Fig. 8, but for (a), (c) potential vorticity  $Q_b$ ; contour interval is  $2 \times 10^{-11} \text{ K m}^2 \text{ s}^{-1} \text{ kg}^{-1}$ ; (b), (d) balanced potential temperature  $\theta_b$ ; contour interval is  $2 \times 10^{-11} \text{ K m}^2 \text{ s}^{-1} \text{ kg}^{-1}$ . Negative values are dashed.

$$E_k = \int_{-X}^{+X} \int_0^{z_T} \rho_0 \left( \frac{|\mathbf{u}_k|^2}{2} + \frac{g^2}{2N^2} \frac{\theta_k^2}{\theta_0^2} \right) dz dx$$

$$= \left\langle \left\langle \rho_0 \left( \frac{|\mathbf{u}_k|^2}{2} + \frac{g^2}{2N^2} \frac{\theta_k^2}{\theta_0^2} \right) \right\rangle \right\rangle, \quad (19)$$

where  $X = 300 \text{ km}$ . In Eq. (19) the indices  $k = l, b$  distinguishes the long disturbance field and the balanced field. We also evaluate the fraction of energy that goes outside of the shear layer  $E_0$  by excluding in Eq. (19) the contribution that comes from the long disturbance field between  $z = z_c - D$  and  $z = z_c + D$ .

The thick line in Fig. 10 shows the temporal evolution of the LSF disturbance energy during the simulation. After  $t \approx 4 \text{ h}$ , which corresponds to the time at which

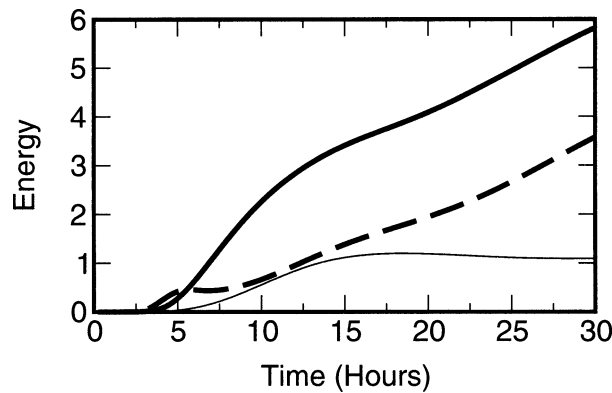


FIG. 10. Disturbance energies evolution when  $H_0 = 15 \text{ m}$ . All energies are divided by  $H_0^3$ . LSF total energy (thick solid line); LSF balanced energy (thick dashed line), and LSF energy outside the shear layer (thin solid line).

GWs have reached a significant amplitude inside the shear layer,  $E_l$  starts to grow rapidly and typically continues until  $t = 10\text{--}15 \text{ h}$ . A closer examination of the different terms that enter the total disturbance energy budget shows that in the first 10 h, the disturbance energy is essentially produced by the work done by the large-scale forcing onto the disturbance field,

$$\langle \langle \rho_0 \mathbf{F}_l \mathbf{u}_b \rangle \rangle, \quad (20)$$

and the balanced flow contributes little to that term. Between 5 and 15 h, the energy growth is essentially due to the conversion of mean kinetic energy to disturbance energy,

$$-\langle \langle \rho_0 u_l w_l U_z \rangle \rangle, \quad (21)$$

a production term that is essentially ageostrophic, with the balanced flow making little contribution to it. It is during that stage that significant IGWs are emitted outside the shear layer, as indicated by the growth of  $E_0$  during that period (thin line in Fig. 10). Although this conversion term is known to be efficient in generating long secondary waves (Farrel and Ioannou 1993; Lott 1997), it does not last in the present configuration. The IGWs coming from the shear layer in Figs. 8a,b are reflected back at the ground and return to the shear layer, where they are absorbed again (Figs. 8d,e). Accordingly, the disturbance kinetic energy production term falls to zero at  $t = 15\text{--}20 \text{ h}$ , and the IGW energy outside of the shear layer  $E_0$  reaches a constant amplitude (thin line in Fig. 10).

After that first 15 h, the disturbance energy growth is essentially due to the conversion of mean available potential energy to disturbance energy:

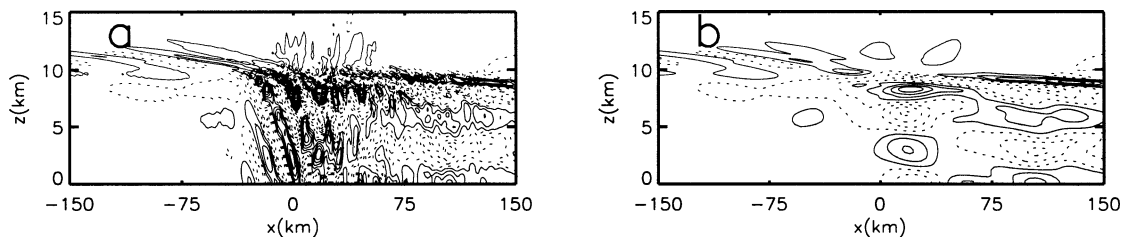


FIG. 11. (a) Total disturbance parallel velocity  $u'(x, z)$  and (b) LSF disturbance parallel velocity  $u_l(x, z)$  at  $t = 30$  h and for  $H_0 = 250$  m. Contour interval  $0.5 \text{ m s}^{-1}$ . Negative values are dashed.

$$\left\langle \left\langle \rho_0 \frac{gfU_z}{\theta_0} v_l \theta_l \right\rangle \right\rangle. \quad (22)$$

This is a pure baroclinic term, essentially due to the balanced flow. It is in good part due to the fact that the LSF transverse velocity  $v_b > 0$  transports mean potential temperature [term  $v_b \theta_y$  in Eq. (C1), appendix C]. Because this transport occurs near where  $U(z) = 0$ ,  $\theta_b$  also decreases [Eq. (C1) in appendix C]. This makes  $v_b \theta_b < 0$  in the shear layer and the available potential energy production term  $> 0$ , according to Eq. (22). Consistent with this, in the long term, the disturbance energy growth is the balanced energy growth (thick dashed line in Fig. 10), and the difference between the disturbance energy  $E_l$  and the balanced energy  $E_b$  is near the IGW energy outside of the shear layer  $E_0$ .

### c. Nonlinear regime: $H_0 = 250 \text{ m}$

When  $H_0$  increases, the dynamics become nonlinear, and the LSF response amplitude compares with the GWs and background flow amplitudes. As an illustration of this, Figs. 11a and 11b compare the total disturbance horizontal velocity field,  $u'(x, z)$  and the filtered disturbance horizontal velocity field  $u_l(x, z)$  at  $t = 30$  h and for  $H_0 = 250$  m. Although the total velocity field is dominated above the mountains by the GWs, the LSF disturbance is clearly evident in most places. For instance, between  $x = 0$  km and  $x = 40$  km and below  $z_c = 10$  km, the LSF disturbance in Fig. 11b makes a

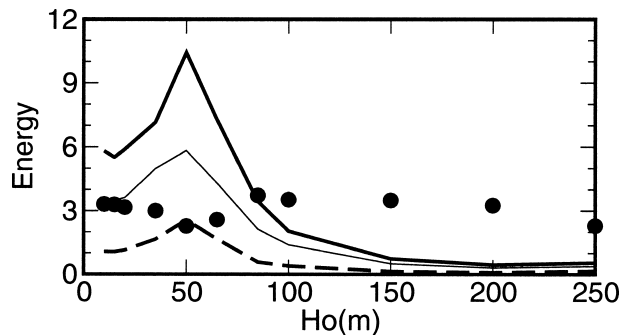


FIG. 12. Disturbance energies as a function of  $H_0$  at  $t = 30$  h. All energies are divided by  $H_0^4$ ; LSF total energy (thick solid line), LSF balanced energy (thick dashed line), and LSF energy outside the shear layer (thin solid line). The dots represent the ratio  $r = E_b/E_0$ .

significant contribution to the total disturbance horizontal velocity field  $u'$  in Fig. 11a. It makes the total disturbance field  $u'(x, z) < 0$  above  $z = 7.5$  km and between  $x = 0$  km and  $x = 40$  km in Fig. 11a. Downstream of the ridge, between  $x = 75$  km and  $x = 150$  km and below  $z = 10$  km, the LSF disturbance field dominates the total disturbance field at near all altitudes.

As a consequence of the substantial modifications of the LSF seen in Fig. 11a, we can expect some feedback onto the GWs themselves. As in the periodic case, these modifications increase the GW reflection at the shear layer, and affect in return the waveforcing  $F_{xl}$ . To illustrate this point, Fig. 12 shows the disturbance energies for different values of  $H_0$ . In the linear case,  $H_0 = 10, 15,$  and  $20$  m;  $E_l/H_0^4$  is near constant, which naturally follows that the LSF disturbance fields  $u_l$  and  $\theta_l$  vary with  $H_0$ , that is, like the GW drag. As  $H_0$  increases— $H_0 = 35, 50,$  and  $65$  m—nonlinearities start to affect the GWs, and the nonlinear reflection increases the waveforcing, the ratios  $E_l/H_0^4$  being significantly larger than the linear case. It is a situation where the fraction of GWs reflected at the shear layer are in such a phase when they arrive at the ground, that they enhance the wave drag. A rather similar mechanism was described by Clark and Peltier (1984) in the nonrotating case. As  $H_0$  increases again— $H_0 = 100, 150, 200,$  and  $250$  m—the nonlinear reflections of the GWs cause the forcings to drop significantly, and the energy of the LSF disturbance becomes around 10 times smaller than that predicted in the linear case. The fact that nonlinear GW reflection can either increase or decrease the waveforcing is not very surprising. As noticed in the periodic case (section 2d), moderately different LSF changes confined to the shear layer can produce reflected GWs with very different phases and amplitudes.

The dots in Fig. 12 present the ratio between the LSF disturbance energy  $E_b$  and the IGWs energy outside of the shear layer  $E_0$ . Contrary to the periodic case, this ratio is near insensitive to the degree of nonlinearities, it is around  $r = 3$  at  $t = 30$  h. Prior to that time it is smaller, which is consistent with the balanced part of the LSF disturbance that keeps increasing in time while the amplitude of the IGWs outside the shear layer stay constant after  $t = 20$  h typically. At  $t = 20$  h, this ratio is near  $r = 2$  (not shown).

#### 4. Conclusions

The fact that the dynamics of gravity waves near critical levels is affected by the Coriolis force has been largely documented in the linear case (Jones 1967; Teitelbaum et al. 1987; Shen and Lin 1999). In this context and for long waves, the dynamics inside the shear layer can be quite different from the nonrotating case analyzed by Booker and Bretherton (1967). The results presented here show that the Coriolis torque also affect the dynamics of rather short GWs, when nonlinear effects are significant. In this case, it is not the primary gravity waves that are directly sensitive to the Coriolis torque, but the LSF they induce when they break. Compared to the nonrotating case, the most obvious difference is that in the periodic nonrotating case, a momentum deposit due to GW breaking produces a regular descent of the large-scale parallel wind, while in the rotating case it is equilibrated by a transverse flow. Still, in the periodic case, GW breaking also produces IOs superimposed onto this transverse flow. The incidence of the Coriolis torque on the LSF response affects the GW dynamics in return. In the periodic case, these feedbacks lead to a resonant loop, which causes the ratio between the amplitude of IOs and that of the transverse flow to far exceed that predicted by the linear theory.

To test the robustness of these findings, we have repeated some of the experiments presented in the paper, changing the model configuration and the GW parameters. For instance, we verified that comparable behavior occurs for a long GW, whose first critical level  $z_{j1}$  is located significantly below  $z_c$  (i.e.,  $z_c - z_{j1} \approx D$ , and  $z_{j1} \ll z_c - l\mu$ ; see appendix B). We also found comparable behavior when the GW reflected at the shear layer is damped artificially near  $z = 0$ , so it does not return toward the shear layer.

The importance of these feedback loops in the nonperiodic case is difficult to address. Simulations that last significantly longer than a day require much CPU time and necessitate a very large domain not to be affected by lateral boundaries, at least when breaking is forced to occur in a background flow with nonzero wind. Nevertheless, we can speculate that comparable feedback loops can occur when GW breaking occurs in a fluid at rest, that is, when the LSF response stay near where the GWs break.

The response to GWs breaking in the nonperiodic case shows two very characteristic patterns. The first is a long-standing wave, which, in our case, stays located below the shear layer. The second is a growing baroclinic disturbance that stays inside the shear layer. When the spatial Rossby number is near 1, these two patterns have comparable amplitude, at least during 1–2 days. Enhancing nonlinearities within moderate bounds does not fundamentally affect the shape, the evolution, and the relative importance of these two patterns. The nonlinearities only cause the GWs to become more or less

efficient in producing LSF disturbances, because the GWs become nonlinearly reflected at the shear layer.

Contrary to the periodic case, we did not test cases where the GWs and the IGWs coming from the shear layer are not reflected by the ground. On the one hand, we can imagine that the balanced response will behave like that presented in the paper, since it essentially results from the fact that GWs deposit momentum there. The amount of momentum deposited is affected by the geometry, but not the general structure of the balanced response. For the IGWs, on the other hand, the structure will be quite different, and the LSF disturbance below the shear layer will present only downward-propagating IGWs. The downward flux of energy associated with these IGWs will be continuously sustained by the kinetic energy production term [Eq. (20)] that falls to zero when the IGWs return to the shear layer in the present paper.

The fact that GW breaking can result in long radiating IGWs supports the interpretation of Scavuzzo et al. (1998), who attributed the presence of IGWs near above the Pyrénées to such a secondary emission. In Scavuzzo et al. (1998) nevertheless, gravity wave forcing was imposed, while here, it is entirely simulated. Another difference with Scavuzzo et al. (1998) is that the results here do not produce large IGWs going into the upper atmosphere. This is due to the fact that long waves have critical levels inside the shear layer where they are absorbed. We can speculate that this would not occur, if the GWs were not breaking at critical levels located in a shear layer.

Although most of the mechanisms presented in this paper are of some importance in the 3D case, it is important to recall that linear studies prove that the 2D response to prescribed body forcing overstates the IOs/IGWs compared to the 3D case (Vadas et al. 2003). This follows that 2D models do not allow the parallel velocity in the LSF response to be in thermal wind balance with a transverse potential temperature gradient. It is very likely that the omission of this balance in the response also has large consequences in the nonlinear cases.

The simulations presented here also show that GWs breaking near critical levels are rather efficient in taking available potential energy from the background baroclinic flow. In the shear layer, this causes GWs to force an LSF disturbance that grows fast, and through a dynamical process that is essentially balanced and that is not due to baroclinic instabilities. In this process, the breaking GWs induce a vertical dipole of PV, which is steered by the vertical shear. This steering causes the positive and negative PV lobes of the dipole to be advected far away from each other. If they were staying above each other, we could speculate that any vertical mixing would tend to damp them.

The ability of GWs to interact with the background flow, at the place where they can efficiently extract available potential energy from the environment, may cause them to play a more significant role in mesoscale and synoptic-scale meteorology than is generally ad-

mitted. In the context of mountain meteorology for instance, it is well known that the surface pressure drag far exceeds the GWs Reynolds stress, which suggests that the large-scale flow (Lott 1995) and the low-level flow dynamics (Lott and Miller 1997) largely overstate the contribution of upper-level GWs in the momentum budget. To a certain extent, the simulations presented in this paper suggest that even a small stress can give rise to a large response.

## APPENDIX A

### Basic Equations and Model

The model uses the 2D anelastic equations described by Scinocca and Shepherd (1992) only modified to include the Coriolis term in the  $f$ -plane approximation. In the model, we split the horizontal velocity field, the potential temperature, and the potential between background and disturbance quantities:

$$\begin{aligned}\mathbf{u} &= U(z)\mathbf{x} + \tilde{\mathbf{u}}(x, z), \\ \theta &= \theta_0(z) + \Theta(y, z) + \tilde{\theta}(x, z), \\ \phi &= \Phi_0(z) + \Phi(y, z) + \tilde{\phi}(x, z).\end{aligned}\quad (\text{A1})$$

In Eq. (A1), the subscript zero refers to the fluid at rest, the tilda to perturbations, and the capital to the background flow. In the following and everywhere in the text, the tilda will be omitted. The background potential temperature field,  $\Theta(y, z)$ , is introduced to maintain the background velocity field in thermal wind balance,

$$\frac{dU}{dz} = -\frac{1}{f} \frac{g}{\theta_0} \frac{\partial \Theta}{\partial y}, \quad (\text{A2})$$

and  $\Phi$  is in hydrostatic balance with  $\Theta$ . With these notations, the anelastic equations for the disturbance fields are written as

$$\begin{aligned}(\partial_t + U\partial_x)\mathbf{u} + U_z w\mathbf{x} + fz \wedge \mathbf{u} + \nabla\phi - g\frac{\theta}{\theta_0}\mathbf{z} \\ = -\mathbf{u}\nabla \cdot \mathbf{u} + \frac{1}{\rho_0}\nabla\mu \cdot \nabla\mathbf{u},\end{aligned}\quad (\text{A3})$$

$$(\partial_t + U\partial_x)\theta + \frac{d\Theta}{dy}v + \frac{d\theta_0}{dz}w = -\mathbf{u} \cdot \nabla\theta + \frac{1}{\rho_0}\nabla\kappa \cdot \nabla\theta, \quad (\text{A4})$$

$$\nabla \cdot (\rho_0 \mathbf{v}) = 0. \quad (\text{A5})$$

Note that in Eqs. (A3)–(A4) the diffusions of the background fields has been neglected because their impact is not of much interest. More significantly, in Eq. (A4), the buoyancy term  $\Theta_z w$  is neglected as well, an approximation that permits the disturbance fields to stay 2D when  $U_z \neq 0$ . It was implicitly assumed by Jones (1967), in this study of linear critical levels with Coriolis force. If we consider a transverse axis  $y$ , this term equals  $-(f\theta_{0y}/g)U_{zz}w$ : it is null in the plane of the simulation located at  $y = 0$ . Comparison with  $\theta_{0z}w$  proves that it becomes significant at a

transverse distance of the plane  $y \approx \text{Ri}_m(U_0/f) = 625$  km, which is significantly larger than the characteristic horizontal scale of the disturbances  $L \approx 100$  km analyzed in this paper.

To parameterize crudely the convective instabilities that can appear in the shear layer, we introduce diffusivities that resemble those used in first-order turbulent closure schemes, but using only the background fields:

$$\mu = \kappa = 0.5(dz)^2|U_z|[1 - \tanh(\text{Ri}/4 - 1)]. \quad (\text{A6})$$

At the top and bottom, the boundary conditions are free-slip and, to force GWs, a linear corrugated bottom at  $z = 0$  is raised smoothly and within  $t_h = 1$  h to impose

$$w'(x, 0, t) = U_0(0)\partial_x H(x). \quad (\text{A7})$$

## APPENDIX B

### Critical Levels Characterization

A steady stationary monochromatic GW with horizontal wavenumber  $k$  often admits three critical levels:

$$\begin{aligned}U(z_c) &= 0, \quad U(z_{j1}) = +f/k, \quad \text{and} \\ U(z_{j2}) &= -f/k,\end{aligned}\quad (\text{B1})$$

when it propagates in a shear flow given by Eq. (2). When  $f = 0$  the incident GW wave is attenuated at  $z_c$  providing the Richardson number  $\text{Ri}(z_c) > 0.25$  and deposit momentum (Booker and Bretherton 1967). In the presence of the Coriolis force, dissipation, and nonlinearities, this result is modified depending on the relative importance of these three processes. To characterize it, it is relevant to introduce the scales

$$\begin{aligned}l_f &= \frac{f}{kU_z(z_c)}, \quad l_\mu = \left[ \frac{\mu}{\rho_0 k U_z(z_c)} \right]^{1/3}, \\ l_N &= \left[ \frac{|A|}{U_z(z_c)} \right]^{2/3},\end{aligned}\quad (\text{B2})$$

which characterize the distance to  $z_c$  of the two inertia  $z_{js}$  critical levels (Jones 1967), the distance to  $z_c$  beyond which one cannot neglect the dissipative terms (Hazel 1967), and the distance to  $z_c$  beyond which one cannot neglect nonlinearities (Lott and Teitelbaum 1992). In Eq. (32),  $|A|$  measures the disturbance amplitude; in our case, it is given by  $|A|^2 = NU_0 H_0^2$ .

In the simulation presented in this paper the viscous scale  $l_\mu \approx 100$  m, which is significantly larger than the model vertical grid spacing in the shear layer ( $dz_{\min} = 30$  m ensuring that the critical-level dynamics is properly solved. Note also that  $l_\mu \ll D$  so GWs absorption remain predicted by the Richardson number at the critical level (Hazel 1967). Furthermore,  $l_f \approx 150$  m  $\approx l_\mu$ , so the three critical levels are linked with each other through dissipative processes, but as  $l_f \ll D$  as well, the GWs behave similarly to the nonrotating case (Teitelbaum et al. 1987). The nonlinear scale  $l_N$  varies be-

tween a few meters and a few hundred meters, that is, from the linear viscous regime  $l_n \ll l_\mu$  to nonlinear viscous ones  $l_n \approx l_\mu$ .

## APPENDIX C

### Balanced Equations

If we assume that the large-scale forcings (a) are small, (b) impose small Rossby numbers, (c) are dominated by  $F_{lx}$ , and (d) give rise to a response whose vertical scale is near  $D$ , the long disturbance Eqs. (17)–(18) are well approximated by the linear hydrostatic set:

$$\begin{aligned} -fv_b + \partial_x \phi_b &= F_{lx}, \\ \partial_z \phi_b - g\theta_b/\theta_0 &= 0, \end{aligned} \quad (C1)$$

$$(\partial_t + U\partial_x)v_b + fu_b = 0,$$

$$(\partial_t + U\partial_x)\theta_b + \Theta_y v_b + \theta_{0z} w_b = 0. \quad (C2)$$

It satisfies a linear quasigeostrophic PV conservation equation

$$\begin{aligned} \rho_0(\partial_t + U\partial_x)Q_b + \rho_0 v_b \partial_y (f\Theta_z/\rho_0) + \rho_0 w_b \partial_z (f\theta_{0z}/\rho_0) \\ = -\nabla \cdot \mathbf{J}_N, \end{aligned} \quad (C3)$$

where the disturbance quasigeostrophic PV,  $Q_b$ , and its nonadvective flux  $\mathbf{J}_N$ , are given by

$$\begin{aligned} \rho_0 Q_b &= (\theta_{0z} \partial_x v_b + f \partial_z \theta_b) \quad \text{and} \\ \mathbf{J}_N &= +(F_{lx} \partial_z \Theta) \mathbf{y} - (F_{lx} \partial_y \Theta) \mathbf{z}, \end{aligned} \quad (C4)$$

respectively. The balanced large-scale flow response can be deduced from  $Q_b$  by using the two balance equations (C1). This results in a linear elliptic equation for  $\phi_b$  that can be inverted assuming the balanced potential temperature is 0 at the model boundaries:

$$\frac{\partial \phi_b}{\partial z} = 0 \quad \text{at } z = 0 \quad \text{and} \quad z = z_T. \quad (C5)$$

## REFERENCES

- Afanasyev, Y. D., and W. R. Peltier, 2001: Numerical simulations of internal gravity wave breaking in the middle atmosphere: The influence of dispersion and three-dimensionalization. *J. Atmos. Sci.*, **58**, 133–153.
- Andrews, D. G., and M. E. McIntyre, 1976: Planetary waves in horizontal and vertical shear: The generalized Eliassen–Palm relation and the mean zonal acceleration. *J. Atmos. Sci.*, **33**, 2031–2048.
- Bacmeister, R. T., and R. T. Pierrehumbert, 1988: On high-drag states of nonlinear flow over an obstacle. *J. Atmos. Sci.*, **45**, 63–80.
- Bessemoulin, P., P. Bougeault, A. Genoves, A. Jansa Clar, and D. Puech, 1993: Mountain pressure drag during PYREX. *Beitr. Phys. Atmos.*, **66** (4), 305–325.
- Blumen, W., 1972: Geostrophic adjustment. *Rev. Geophys.*, **10**, 485–528.
- Booker, J. R., and F. P. Bretherton, 1967: The critical layer for internal gravity waves in a shear flow. *J. Fluid Mech.*, **25**, 513–529.
- Bretherton, F. P., 1969: Momentum transport by gravity waves. *Quart. J. Roy. Meteor. Soc.*, **95**, 213–243.
- Buhler, O., M. E. McIntyre, and J. F. Scinocca, 1999: On shear-generated gravity waves that reach the mesosphere. Part I: Wave generation. *J. Atmos. Sci.*, **56**, 3749–3763.
- Clark, T. L., and W. R. Peltier, 1984: Critical level reflection and the resonant growth of nonlinear mountain waves. *J. Atmos. Sci.*, **41**, 3122–3134.
- Eliassen, A., and E. Palm, 1961: On the transfer of energy in the stationary mountain waves. *Geophys. Publ.*, **22** (3), 1–23.
- Farrel, B. F., and P. J. Ioannou, 1993: Transient development of perturbations in stratified shear flow. *J. Atmos. Sci.*, **50**, 2201–2214.
- Ford, R., 1994: Gravity wave radiation from vortex trains in rotating shallow waters. *J. Fluid Mech.*, **281**, 81–118.
- Fritts, D. C., 1978: The nonlinear gravity wave-critical level interaction. *J. Atmos. Sci.*, **35**, 397–413.
- , and Z. Luo, 1992: Gravity wave excitation by geostrophic adjustment of the jet stream. *J. Atmos. Sci.*, **49**, 681–697.
- , T. L. Palmer, O. Andreassen, and I. Lie, 1996: Evolution and breakdown of Kelvin–Helmoltz billows in stratified compressible flows. Part I: Comparison of two- and three-dimensional flows. *J. Atmos. Sci.*, **53**, 3173–3212.
- Hamming, R. W., 1983: *Digital Filters*. Prentice-Hall, 257 pp.
- Haynes, P. H., and M. E. McIntyre, 1987: On the evolution of vorticity and potential vorticity in the presence of diabatic heating and frictional or other forces. *J. Atmos. Sci.*, **44**, 828–841.
- Hazel, P., 1967: The effect of viscosity and heat conduction on internal gravity waves at a critical level. *J. Fluid Mech.*, **30**, 775–783.
- Holton, J. R., 1982: The role of gravity wave-induced drag and diffusion in the momentum budget of the atmosphere. *J. Atmos. Sci.*, **39**, 791–799.
- Jones, W. L., 1967: Propagation of internal gravity waves in fluids with shear flow and rotation. *J. Fluid Mech.*, **30**, 439–448.
- Lott, F., 1995: Comparison between the orographic response of the ECMWF model and the PYREX 1990 data. *Quart. J. Roy. Meteor. Soc.*, **121**, 1323–1348.
- , 1997: The transient emission of propagating gravity waves by a stably stratified shear layer. *Quart. J. Roy. Meteor. Soc.*, **123**, 1603–1619.
- , and H. Teitelbaum, 1992: Nonlinear dissipative critical level interaction in a stratified shear flow: Instabilities and gravity waves. *Geophys. Astrophys. Fluid Dyn.*, **66**, 133–167.
- , and M. Miller, 1997: A new subgrid scale orographic drag parameterization: Its testing in the ECMWF model. *Quart. J. Roy. Meteor. Soc.*, **123**, 101–127.
- Miranda, P. M. A., and I. A. James, 1992: Non-linear three dimensional effects on gravity-wave drag: Splitting flow and breaking waves. *Quart. J. Roy. Meteor. Soc.*, **118**, 1057–1081.
- O’Sullivan, D., and T. J. Dunkerton, 1995: Generation of inertia gravity waves in a simulated life cycle of baroclinic instability. *J. Atmos. Sci.*, **52**, 3695–3716.
- Palmer, T. N., G. J. Shutts, and R. Swinbank, 1986: Alleviation of systematic westerly bias in general circulation and numerical weather prediction models through an orographic gravity wave drag parametrization. *Quart. J. Roy. Meteor. Soc.*, **112**, 2056–2066.
- Pierrehumbert, R. T., and B. Wyman, 1985: Upstream effects of mesoscale mountains. *J. Atmos. Sci.*, **42**, 977–1003.
- Reeder, M. J., and M. Griffiths, 1996: Stratospheric inertia-gravity waves generated in a numerical model of frontogenesis. Part I: Model solutions. *Quart. J. Roy. Meteor. Soc.*, **122**, 1153–1174.
- Rossby, C. G., 1937: On the mutual adjustment of pressure and velocity distributions in certain simple current systems. *J. Mar. Res.*, **21**, 15–28.
- Scavuzzo, C. M., M. A. Lamfri, H. Teitelbaum, and F. Lott, 1998: A study of the low frequency inertia-gravity waves observed during PYREX. *J. Geophys. Res.*, **103** (D2), 1747–1758.
- Schär, C., and D. R. Durran, 1997: Vortex formation and vortex shedding in continuously stratified flows past isolated topography. *J. Atmos. Sci.*, **54**, 534–554.
- Scinocca, J. F., and T. G. Shepherd, 1992: Nonlinear wave activity

- conservation laws and Hamiltonian structure of the two-dimensional anelastic equations. *J. Atmos. Sci.*, **49**, 5–27.
- Shen, B. W., and Y. L. Lin, 1999: Effects of critical levels on two-dimensional back sheared flow over an isolated mountain ridge. *J. Atmos. Sci.*, **56**, 3286–3302.
- Smith, R. B., 1985: On severe downslope winds. *J. Atmos. Sci.*, **42**, 2597–2603.
- Teitelbaum, H., H. Kelder, and C. A. van Duin, 1987: Propagation of internal gravity waves in a rotating fluid with shear flow. *J. Atmos. Terr. Phys.*, **49**, 413–420.
- Vadas, S. L., and D. C. Fritts, 2001: Gravity wave radiation and mean responses to local body forces in the atmosphere. *J. Atmos. Sci.*, **58**, 2249–2279.
- , ———, and M. J. Alexander, 2003: Mechanism for the generation of secondary waves in wave breaking regions. *J. Atmos. Sci.*, **60**, 194–214.